A CFD Case Study of a Fan Stage With Split Flow Path Subject to Total Pressure Distortion Inflow

Wai-Ming To
University of Toledo, Toledo, Ohio

NASA STI Program . . . in Profile

Since its founding, NASA has been dedicated to the advancement of aeronautics and space science. The NASA Scientific and Technical Information (STI) Program plays a key part in helping NASA maintain this important role.

The NASA STI Program operates under the auspices of the Agency Chief Information Officer. It collects, organizes, provides for archiving, and disseminates NASA's STI. The NASA STI Program provides access to the NASA Technical Report Server—Registered (NTRS Reg) and NASA Technical Report Server—Public (NTRS) thus providing one of the largest collections of aeronautical and space science STI in the world. Results are published in both non-NASA channels and by NASA in the NASA STI Report Series, which includes the following report types:

- TECHNICAL PUBLICATION. Reports of completed research or a major significant phase of research that present the results of NASA programs and include extensive data or theoretical analysis. Includes compilations of significant scientific and technical data and information deemed to be of continuing reference value. NASA counter-part of peer-reviewed formal professional papers, but has less stringent limitations on manuscript length and extent of graphic presentations.

- TECHNICAL MEMORANDUM. Scientific and technical findings that are preliminary or of specialized interest, e.g., "quick-release" reports, working papers, and bibliographies that contain minimal annotation. Does not contain extensive analysis.

- CONTRACTOR REPORT. Scientific and technical findings by NASA-sponsored contractors and grantees.

- CONFERENCE PUBLICATION. Collected papers from scientific and technical conferences, symposia, seminars, or other meetings sponsored or co-sponsored by NASA.

- SPECIAL PUBLICATION. Scientific, technical, or historical information from NASA programs, projects, and missions, often concerned with subjects having substantial public interest.

- TECHNICAL TRANSLATION. English-language translations of foreign scientific and technical material pertinent to NASA's mission.

For more information about the NASA STI program, see the following:

- Access the NASA STI program home page at http://www.sti.nasa.gov

- E-mail your question to help@sti.nasa.gov

- Fax your question to the NASA STI Information Desk at 757-864-6500

- Telephone the NASA STI Information Desk at 757-864-9658

- Write to:
  NASA STI Program
  Mail Stop 148
  NASA Langley Research Center
  Hampton, VA 23681-2199

NASA/CR—2017-219698

A CFD Case Study of a Fan Stage With Split Flow Path Subject to Total Pressure Distortion Inflow

Wai-Ming To
University of Toledo, Toledo, Ohio

National Aeronautics and
Space Administration

Glenn Research Center
Cleveland, Ohio 44135

November 2017

Level of Review: This material has been technically reviewed by expert reviewer(s).

Available from

NASA STI Program
Mail Stop 148
NASA Langley Research Center
Hampton, VA 23681-2199

National Technical Information Service
5285 Port Royal Road
Springfield, VA 22161
703-605-6000

This report is available in electronic form at http://www.sti.nasa.gov/ and http://ntrs.nasa.gov/

A CFD Case Study of a Fan Stage With Split Flow Path Subject to Total Pressure Distortion Inflow

Wai-Ming To
University of Toledo
Toledo, Ohio 43606

Abstract

This report is the documentation of the work performed under the Hypersonic Project of the NASA's Fundamental Aeronautics Program. It was funded through Task Number NNC10E444T under GESS-2 Contract NNC06BA07B. The objective of the task is to develop advanced computational tools for the simulation of multi-stage turbomachinery in support of aeropropulsion. This includes work elements in extending the TURBO code and validating the multi-stage URANS (Unsteady Reynolds Averaged Navier Stokes) simulation results with the experimental data. The unsteady CFD (Computation Fluid Dynamics) calculations were performed in full wheel mode with and without screen generated total pressure distortion at the computational inflow boundary, as well as in single passage phase lag mode for uniform inflow. The experimental data were provided by NASA from the single stage RTA (Revolutionary Turbine Accelerator) fan test program.

Introduction

Significant non-uniform flow condition at the fan-face of the aeropropulsion system is frequently encountered in many of the advanced aerospace vehicles. These propulsion systems can be either a podded or an embedded design employed in HWB (Hybrid Wing Body) airframe concept. It is also a topic of interest in military applications, in which advanced air vehicles have already deployed some form of embedded propulsion systems in their design because of the requirements of compact and low observable inlets. Even in the conventional airframe/engine design, the fan could operate under such condition when the air vehicle is undergoing rapid maneuvering action. It is believed that a better understanding of the fan's aerodynamic and aeromechanical response to this type of operating condition or off design operation would be beneficial to designing distortion tolerant blades for improved engine operability.

The objective for this research is to assess the capability of turbomachinery code as an analysis tool in understanding the effects and evaluating the impact of flow distortion on the aerodynamic and aeromechanical performance of the fan in advanced propulsion systems. Results from the testing of an advanced fan stage released by NASA are available and will be used here for CFD code validation. The experiment was performed at NASA's high speed compressor facility as part of the RTA (Revolutionary Turbine Accelerator) demonstration project, a joint effort of NASA Glenn Research Center and GE Aircraft Engines in developing an advanced Mach 4 TBCC (Turbine Based Combined Cycle) turbofan/ramjet engine for access to space. Part of the test was to assess the aerodynamic performance and operability of the fan stage under non-uniform inflow condition. Various flow distortion patterns were created at the fan-face by manipulating sets of screens placed upstream of the wind tunnel. Measurements at the fan-face will provide the necessary distortion flow information as the inflow boundary condition for the CFD in a full wheel simulation. Therefore the purpose of this work is to demonstrate the NASA supported multi-stage turbomachinery code, TURBO [1-5], in the aerodynamic performance analysis of a modern fan design operating under off design condition, and in particular to validate the CFD results with the RTA fan test data.

A brief description of the RTA fan rig configuration is given in the next section, explaining on how flow distortion were measured in the test and constructed for the CFD at the fan-face. It is followed by a section summarizing previous CFD work performed at NASA relevant to the current fan configuration. A short description of the TURBO code is given next, followed by details in the computational model of the fan rig, the required computing resources, and the numerical procedure for the simulations. The CFD results are presented in the discussion section and finally concluding remarks are summarized.

RTA Fan Rig

The fan stage designed for the NASA rig test is a 57% scale of the demonstrator engine for the RTA project. It has a diameter of 0.5588 m. The rotor's rotational speed is 17,280 rpm with a tip speed of about 506 m/s at 100% design speed. Behind the rotor is a closely coupled variable OGV designed for simulating high Mach number flight conditions. The rotor-OGV has a blade count of 25-48. Following the OGV, the flow path is split by a radial splitter, held together with 6 integrated fan frame struts, that extends to the exhaust vents simulating the core and the bypass flow paths of the engine. Description of the rig design and detailed information on the tests and instrumentation can be found in [6].

Two liners over the rotor were tested in the experiment to investigate casing wall treatment, however, only the smooth liner case is considered here for the CFD analysis. OGV "exit plane" measurements were made with a set of probes at a distance roughly 50% of the OGV axial cord downstream of the trailing edge, indicated by the yellow line marked STA21 in Figure 1. Eight instrumented rakes (indicated by the angular positions in blue boxes in Figure 5) were mounted on the casing wall, taking measurements from 7 spanwise positions. Comparison of the CFD results with the experimental data will be made on this rating plane.

To create various flow distortion pattern at the fan-face, different sets of screens placed upstream of the wind tunnel were used in the experiment, generating a total pressure deficit of over 10% going into the fan. In this paper, only the total pressure distortion map generated by the "sinusoidal" screen set (shown in Figure 3), simulating the effect of serpentine duct flow, is considered. The screen set was orientated in different position to complete a full circle measurement. Six instrumented rakes (indicated by the angular positions in blue boxes in Figure 3b) were mounted to the casing wall taking measurements for each orientation.

In this paragraph, the procedure of constructing the inflow total pressure distortion map for the CFD is described. Referring to Figure 3, the convention adopted for the 0˚ is the 3 o'clock position front-looking-aft and counterclockwise for positive angles. Total pressure were measured with the 6 inlet rake probes and a boundary layer probe for the 4 screen orientations by rotating the set by 0˚, 90˚, 180˚, and 270˚ (referred to the S0, S90, S180, and S270 respectively). For example, Figure 3a illustrates a screen set in 0˚ or S0 orientation. There were 6 inlet rakes, each one of them had 8 spanwise measurements that resulted in a measurement grid of 24 by 8 (shown as

grid lines in grey in Figure 3b) in a full circle. Similarly, the 6 spanwise measurements from the single boundary layer probe located at the 170˚ position produces boundary layer total pressure data at 170˚, 260˚, 350˚, and 80˚ positions for the S0, S90, S180, S270 screen orientations. The total pressure map (in colored contour lines as well) constructed from patching the boundary layer profile to the inlet rake measurements is shown in Figure 3b. Also plotted in the same figure is the total pressure map (in white contour lines) interpolated from the measurement grid on to the computational mesh that consists of 5 blocks in the straight duct section (see Figure 2). The computational mesh of one such block, 81 radial and 51 tangential points, is indicated in the figure.

The uniform inflow situation involves a single radial measurement. Figure 4 shows the total pressure measurements from the boundary layer and the inlet rake probes for 2 test conditions, R642 and R644. The averaged total pressure from the 2 probes were used for the common points when patching the data. The result for the composite total pressure contour is shown in the inset of the diagram.

In this report, experimental and CFD results are presented for the 80% design speed.

Previous Related CFD Work

Steady flow computation for this fan rig had been reported in [7] for speeds ranging from 37% to 100%, where APNASA code was used to conduct the CFD analysis. It is a single passage multi-stage analysis assuming uniform flow condition at the fan-face. Valuable information about the blade geometry and rotor tip clearance uncovered from the the analysis were incorporated into the computational geometry of the present study.

The type of distortion flow considered here renders the single passage computation inappropriate. In a joint effort between NASA Glenn Research Center and Honeywell Aerospace under the VAIIPR (Versatile Affordable Integrated Inlet-Fan for Performance and Reliability) program, CFD analysis of a 1½ stage fan rig of Honeywell design was conducted with full wheel simulations using the TURBO code, in which the effect of rod generated flow distortion on the fan's aerodynamic and aeromechanical response was investigated. The rig configuration differs from this fan rig in that the rotor was mounted on a constant radius spinner instead of a conical spinner. The distortion flow was generated by a 2-rod arrangement with a total pressure deficit of 3% measured at the fan-face. A similar computational approach is followed here in the full wheel simulations of the RTA fan.

TURBO Code

The TURBO code, which is widely accepted for aerodynamic and aeroelastic analysis [8-10] in turbomachinery community, is used for the current RTA fan study. The version used in this work is TURBO Parallel Version 4 [5]. It is a MPI implemented multi-block, structured grid, turbomachinery flow simulation code capable of treating general multi-stage configurations, by solving the 3-D compressible unsteady Reynolds-Averaged Navier-Stokes equations in Cartesian coordinate system. It uses the high Reynolds number form of the k-ε turbulence model with wall damping function for the eddy viscosity [11]. Real gas effect is modeled with variable specific heat ratio, γ, as a function of temperature via lookup table. The governing equations are cast in the relative frame of reference of the blades with the velocity vector formed in the absolute frame basis [3]. They are discretized with an implicit time marching cell-centered finite volume formulation, and the solution algorithm for the non-linear algebraic equations is the Newton's method. A symmetric Gauss-Seidel relaxation scheme is used for the matrix solution in each of the Newton's iteration. A characteristics-based flux-vector splitting high order upwind scheme is employed for the convection terms. Details of the numerical method can be found in [12]. Online TURBO documentation can be found from http://www.simcenter.msstate.edu/docs/msu_turbo.

Version 4 was modified to allow engine configuration with multiple exit flow paths which is common for modern turbofan engines. Static pressure at the hub or at the casing is specified at the exit boundary assuming radial equilibrium flow condition. The exit static pressures are adjusted independently until a desired bypass ratio is achieved. Although mass flow exit throttle condition is available in TURBO, the calculation is sometimes numerically unstable due to its dependence and interaction with the evolving exit flow. The total condition preserving inflow boundary condition implemented in TURBO, simulating the incoming boundary layer with a radial profile, is extended here to allow radial and circumferential varying total pressure and total temperature condition. Variable flow angles information can also be incorporated in the boundary condition if they are available from the experiment.

Computational Model of the RTA Fan Rig

Figure 1 shows the schematics of the RTA fan configuration used for the computation. It is partitioned into 4 blocks or blade rows, a straight circular duct section, followed by the rotor and the OGV blade rows with the strut row behind them. The stationary blocks are shown in blue or light blue and the rotating block in red, with blades highlighted in grey. The exit boundary is chosen at

a downstream axial plane such that the radial equilibrium flow condition can be applied. The inflow boundary is positioned at an axial plane close to the inflow measurement plane, about 7 axial cord length from the rotor. Zero flow angles are assumed in the computation because of lack of information from the experiment.

The total pressure distortion pattern from Figure 3b, constructed from the measurements, is prescribed as the inflow boundary condition in the computation. It is assumed to be static and held fixed in the simulations. In reality, the inlet-fan interaction is dynamic in nature. The action of the fan produces a "pumping" effect on the inlet flow that would locally reduce adverse pressure gradients, induce swirl, and distribute total pressure distortion. The total pressure distortion from the inlet in turn affects the performance and stability margin of the fan. In the rig test, the experiment began taking data when the flow had established itself and so the total pressure data can be considered to be static for computational purpose.

Measurements indicated that the temperature variation was less than 2.5°K at the fan-face from the screen generated distortion test. There was not enough information about the temperature distribution from the test, so the total temperature is assumed to be constant at the inflow boundary.

In addition, turbulence intensity of 1.5% and an eddy viscosity of 100 (normalized by the laminar viscosity) are used as inflow boundary condition.

The rotor has a tip clearance of 0.0254 cm and the variable OGV has a tip and hub clearance of 0.0381 cm. There is no clearances in the strut. The clearance gap region can be gridded up and computed directly if so desired, instead the clearance model is used here for its computational efficiency, robustness, and reliability. It is modeled as a lossless orifice across the opening with a flow discharge coefficient of 1.0 [13,14]. Usually 4 to 6 cells were used in the computation. Boundary condition for the walls is assumed to be impermeable no-slip adiabatic and no leakage flow is assumed in the computation.

The straight duct section consists of 5 blocks, each has a mesh dimension of (39,81,51) in the axial, radial, and circumferential direction. Mesh dimensions for each of the rotor, OGV, and the strut core and bypass passages are (169,81,51), (133,81,51), (156,41,201), and (156,41,201) respectively, of which there are 60 to 85 axial cells between the leading edge and trailing edge of the blade, totaling 52 million cells for the whole wheel. Figure 2 shows the block structure used in the 230-block full wheel simulation optimized for the mesh size of the blocks and the memory constraint of the hardwares. It has a load balance of 89%.

Computations were performed on the Pleiades compute cluster at NASA's advanced supercomputing facility. Each node consists of 8 cores with 8 GB of shared memory. The single block per

processor approach requires 230 cores for each batch job. For a complete revolution of 2000 time steps, it took about 8 hours to finish.

Convergence is dependent on the initial condition and the precision of the bypass ratio of the solution. It could take up to 50 revs. In particular, the process of starting from scratch is significantly longer, requiring a combination of smaller time step (or CFL number) to begin with and spinning up the rotor to get past the numerical transient. Nearing stall is also a time consuming process because of the sensitivity to the back pressure settings where a slight adjustment in pressure could cause the computation stalling the fan. The computation usually starts from the closest last-computed operating point on the speed line. When starting from scratch because of no reasonable initial flow available, it is usually more convenient to begin from the choke side and gradually move up along the speed line to the target operating point.

Discussion of Results

The computation were conducted at 80% design speed. Results from both uniform inflow and total pressure distortion inflow are presented in this section. Single passage phase lag computation were also performed for the uniform inflow cases and compared with the full wheel simulation results. Data comparison were made on the rating plane STA21 (see Figure 1) behind the OGV. There are 8 fixed rakes mounted on the casing wall, each taking measurements of 7 spanwise positions. Figure 5 is a schematic showing the angular positions of the OGV rake. Test data presented here are simple arithmetic average from these probe readings. For the uniform inflow case, they are represented by the the black lines in the figure. They are also marked with the rake's angular position in blue boxes. Rake positions relative to the screen orientation are also shown in the figure as colored lines for the distortion inflow case.

Uniform Inflow

Four operating points on the speed line were computed for the uniform inflow corresponding to test readings R642, R645, R648, and R649, with additional points computed with single passage simulations to complete the speed line. Table 1 is a quantitative comparison of the overall performance data between the measurements and the 2 CFD results for the 4 cases. Results for the total pressure ratio and adiabatic efficiency are also plotted in Figure 6. The CFD performance data were computed at each time step and averaged over 2 revolutions (direct averaging), shown as the squares and diamonds in solid colors in the figure. Both the single passage and the full wheel simulations display similar trend, with the CFD results over-predicting the data. The choke mass flow rate, computed from the single passage simulation, is also over-predicted.

An alternative way of computing the performance data is by taking the time averaged of the flow field first and then computing them only at those spatial locations where probe measurements were made. For full wheel simulations, the average was computed from the probe positions and for phase lag simulations it was simply circumferentially averaged. The difference between the 2 methods of computing the average performance data is whether the time average is taken before or after the performance data calculation. The second difference is whether the result is integrated over the the flow area or a simple arithmetic average of all points.

The results for the second average method are also plotted in Figure 6 as shaded squares and diamonds. It can be seen that these "probe-position" averaged data are always lower than the direct averaged data. The difference between them is more pronounced near choke and near stall where stronger flow non-uniformity and unsteadiness is present.

Figure 7 to Figure 9 show the comparison of total pressure contour from the full wheel simulations at an instant in time and the time averaged results for 3 of the 4 cases representative of near design (R642), near choke (R645) and near stall (R649). The time averaged solutions show little variation from passage to passage, whereas the instantaneous ones clearly show some spatial wave structures.

Radial profiles of "direct" averaged total pressure and total temperature at STA21 are plotted in Figure 10 for the 4 cases presented in Table 1. Both the full wheel and the phase lag results are very similar and over-predict the data. Comparison of "direct" averaged and "rake-position" averaged results from full wheel simulations are shown in Figure 11. The difference between the 2 averaging methods for uniform inflow is not very significant particularly for the temperature.

"Sinusoidal" Screen Generated Distortion Inflow

Following the same data reduction procedure and using the same convention as described in the previous sections, the "sinusoidal" screen generated distortion inflow (or simply distortion inflow) results are presented in this section. The total pressure map from Figure 3b was normalized by its average and fixed at the boundary in the simulations with constant temperature and zero flow angles. As discussed in the previous section on inflow boundary condition, the choice for this simplified condition in the CFD stems from the computational necessity and the lack of complete flow definition at the fan-face. For this matter, the simulation results shall be viewed as qualitative when comparing to the test data.

Three operating points on the speed line for the near design, near choke, and near stall conditions were computed with full wheel simulations applying the same total pressure distortion pattern at the inflow boundary. Overall performance data are shown in Table 2 with the test data. They are

also plotted in Figure 12 for the total pressure ratio and adiabatic efficiency. The uniform inflow data are repeated in the figure for reference. Data from each screen orientation are shown in shaded triangles. There are some scattering in the test data but the ones for the 90˚ screen are clearly the anomalies and were discarded when averaging the test data. They are the readings from rake positions colored in red in Figure 5. But readings from the inlet rake probes are not affected by this inconsistency so that the total pressure distortion data is reliable and can be used as the boundary condition for the CFD. Specifically, referring to Figure 3b, the S90 screen orientation contributing to probe readings at 20˚, 60˚, 140˚, 220˚, 300˚, and 340˚ do not exhibit any discontinuities in the contour lines from the data. Hence, the S90 OGV rake measurements were dropped from the analysis while keeping all of the inlet rake total pressure measurements. The experimental performance data shown in Table 2 is the result of averaging the OGV rake measurements from the S0, S180, and S270 screen orientations.

The CFD results also over-predicted the data for the distortion inflow. Unlike the uniform inflow case, the probe-position averaging data are higher than those computed with direct averaging method. This is probably attributed to the larger spatial non-uniformity resulted from the distortion inflow that persisted downstream of the OGV (see Figure 13 to Figure 15). Comparing Figure 12 to Figure 6, the effect of the distortion inflow is the lowering of the speed line as shown from both the CFD and the test data.

Total pressure contours at STA21 for an instantaneous and for the time averaged solutions of the 3 computed cases are shown in Figure 13 to Figure 15 for the near design (R1947-R1951), near choke (R1957-R1961), and near stall (R1962-R1966) cases. The time averaged fields exhibit remarkably similar flow features to their respective instantaneous fields. The low pressure pockets near the hub in the diagrams are the signatures of the separated flow in the stator passages. For the near design and near stall case, the low pressure pockets, originated from the low pressure sector of the inflow are persistent and do not mix out occupying more or less in the same sector as they were at the inflow. At the same time, the high pressure pockets have drifted from the 9 o'clock sector towards the 12 o'clock sector. However, the near choke case is very different. Although the size is much reduced compared with the other 2 cases, the low pressure pockets in the low pressure sector is still present from the contour plot. While the flow for most of the stator passages from the the high pressure sector is choked in this case, the flow in the low pressure sector is not. This can be seen from Figure 21 that there are usually flow separation pockets following the supersonic flow in the stator passages. The low pressure pockets near the hub in the high pressure sector are the footprints of the separated flow in the stator passages.

Comparing to the uniform inflow results, significant flow non-uniformity from passage to passage is seen for the distortion inflow cases. This could be an important issue in the consideration of the placement of probes when taking the fan's aerodynamic performance measurements.

Total pressure radial profiles at STA21 for the 3 cases are shown in Figure 16. The rake-position averaged results indicate larger swing than the direct averaged ones, but both over-predict the data generally.

Flow Features

Supersonic and separated flow regions in the flow field are shown in Figure 17 to Figure 19 for the time averaged uniform inflow simulation results for the near design (R642), near choke (R645), and near stall (R649) cases. A front view and side views of 0˚, 90˚, 180˚, and 270˚ are shown in the figure for each case, side by side with their respective total pressure contour plot at STA21. Similar plots for the time averaged distortion inflow results for the near design (R1947-R1951), near choke (R1957-R1961), and near stall (R1962-R1966) cases are shown in Figure 20 to Figure 22. The low pressure sector in the distortion inflow cases is shown in the figures bounded between the yellow and the blue bands. The supersonic regions are highlighted in green and the flow separation region in red. The rotor blades and the casing are removed for visual clarity. At this speed (80% design speed), the rotor blade tip is transonic. Flow reversal in the rotor tip clearance can be seen from the figures.

The flow for the uniform inflow near design case (Figure 17) is free of any significant supersonic or flow separation pockets relative to the near choke and near stall cases. For the distortion inflow case (Figure 20), the stator passages that lie in the path of the low pressure sector have some flow separation pockets, while others from the high pressure sector are partially choked. A distinct flow separation region can be seen on the casing behind those stators in the low pressure sector.

On the choke side, the flow is nearly filled with supersonic pockets in the stator passages as can be seen from Figure 18 and Figure 21. For the uniform inflow, supersonic pockets are formed in all of the stator passages. In the case of distortion inflow, the supersonic pockets appear in all of the stator passages except for those lying in the low pressure sector. Separated flow can be seen following the supersonic pockets.

On the stall side, Figure 19 shows the flow separation pockets are building up in the strut passages and along the lip of the radial splitter for the uniform inflow. For the distortion inflow shown in Figure 22, the picture is very similar to the near design case with slightly larger separated flow pockets and shrinking supersonic pockets in the stator passages.

Summary and Concluding Remarks

TURBO was demonstrated as a viable CFD tool for analyzing the aerodynamic performance of an advanced fan design operating at off design condition in a moderately complex rig configuration. Full wheel computation of the RTA fan stage was achieved with modest number of processors. Simulations for uniform and distortion inflow were performed at various operating conditions for the 80% speed. Comparison with the test data shows that the fan's pressure ratio and adiabatic efficiency were over-predicted by the CFD. Total pressure and total temperature at the OGV rating plane were also over-predicted. The time averaged solutions for the uniform inflow show little passage to passage variation. A greater flow non-uniformity is observed for the distortion inflow cases. In particular, they can be traced to the distortion flow from the inflow boundary.

References

1. Janus, J.M. and Whitfield, D.L., "A Simple Time-Accurate Turbomachinery Algorithm With Numerical Solutions of an Uneven Blade Count Configuration," AIAA-89-0206, 1989.

2. Chen, J.P. and Whitfield, D.L., "Navier–Stokes Calculations for the Unsteady Flowfield of Turbomachinery," AIAA-93-0676, 1993.

3. Chen, J.P., Ghosh, A.R., Sreenivas K., and Whitfield, D.L., "Comparison of Computations Using Navier-Stokes Equations in Rotating and Fixed Coordinates for Flow Through Turbomachinery," AIAA-97-0878, 1997.

4. Chen, J.P. and Barter, J.W., "Comparison of Time–Accurate Calculations for the Unsteady Interaction in Turbomachinery Stage", AIAA–98–3292, July, 1998.

5. Chen, J.P. and Briley, W.R., "A Parallel Flow Solver for Unsteady Multiple Bladerow Turbomachinery Simulations," ASME-2001-GT-0348, 2001.

6. Suder, K.L., Prahst, P.S., and Thorp, S.A., "Results of an Advanced Fan Stage Operating Over a Wide Range of Speed and Bypass Ratio, Part I: Fan Stage Design and Experimental Results," ASME-GT-2010-22825, 2010.

7. Celestina, M.L., Suder, K.L., and Kulkarni, S., "Results of an Advanced Fan Stage Operating Over a Wide Range of Speed and Bypass Ratio, Part II: Comparison of CFD and Experimental Results," ASME-GT2010-23386, 2010.

8. Van Zante, D.E., To, W.M., and Chen, J.P., "Blade Row Interaction Effects on the Performance of a Moderately Loaded NASA Transonic Compressor Stage," ASME-GT-2002-30575, 2002.

9. Chen, J.P., Hathaway, M.D., Herrick, G.P., and Skoch, G.J., "Numerical Simulation of Stall and Stall Control in Axial and Radial Compressors," AIAA-2006-0418, 2006.

10. Srivastava, R., Bakhle, M., and Keith, T.G., "Numerical Simulation of Aerodynamic Damping for Flutter Analysis of Turbomachinery Blade Rows," Journal of Propulsion and Power, pp. 260-267, Vol. 19, No. 2, 2003.

11. Zhu, J. and Shih, T.H., "CMOTT Turbulence Module for NPARC," NASA Report No. CR 204143, 1997.

12. Chen, J.P., "Unsteady Three-Dimensional Thin-Layer Navier-Stokes Solutions for Turbomachinery in Transonic Flow," Ph.D. thesis, Mississippi State University, 1991.

13. Shabbir, A., Adamczyk, J.J., Strazisar, A.J., and Celestina, M.L., "The Effect of Hub Leakage Flow on Two High Speed Axial Floe Compressor Rotors," ASME-97-GT-346, 1997.

14. Van Zante, D.E., Strazisar, A.J., Wood, J.R., Hathaway, M.D., and Okiishi, T.H., "Recommendations for Achieving Accurate Numerical Simulation of Tip Clearance Flows in Transonic Compressor Rotors," ASME J. of Turbomachinery, pp. 733-743, Vol. 122, No. 4, October 2000.

Tables

TEST READING	CORRECTED INLET FLOW (KG/S)	PRESSURE RATIO	ADIABATIC EFFICIENCY	BYPASS RATIO
R642 Full Wheel Phase Lag	28.2335 28.2606 28.2278	1.8551 1.9079 1.9103	0.8574 0.8943 0.8964	0.7351 0.7336 0.7350
R645 Full Wheel Phase Lag	30.4421 30.4527 30.4574	1.7177 1.8355 1.8375	0.8146 0.8955 0.8968	1.2240 1.2175 1.2260
R648 Full Wheel Phase Lag	26.7221 26.7516 26.7178	1.8730 1.9318 1.9343	0.8379 0.8764 0.8784	0.6105 0.6133 0.6102
R649 Full Wheel Phase Lag	25.3616 25.3479 25.3336	1.8734 1.9436 1.9443	0.8109 0.8546 0.8565	0.5348 0.5116 0.5342

Table 1. Comparison of Uniform Inflow Simulation Results for 4 Operating Points.

TEST READING	CORRECTED INLET FLOW (KG/S)	PRESSURE RATIO	ADIABATIC EFFICIENCY	BYPASS RATIO
R1947 - R1951 TURBO	28.3661 28.4002	1.8344 1.8668	0.8684 0.8742	0.8137 0.8710
R1957 - R1961 TURBO	29.5230 29.8485	1.7860 1.8221	0.8638 0.8703	0.9558 1.3594
R1962 - R1966 TURBO	26.9395 26.7725	1.8546 1.8743	0.8458 0.8513	0.7202 0.8182

Table 2. Comparison of Distortion Inflow Simulation Results.

Figures
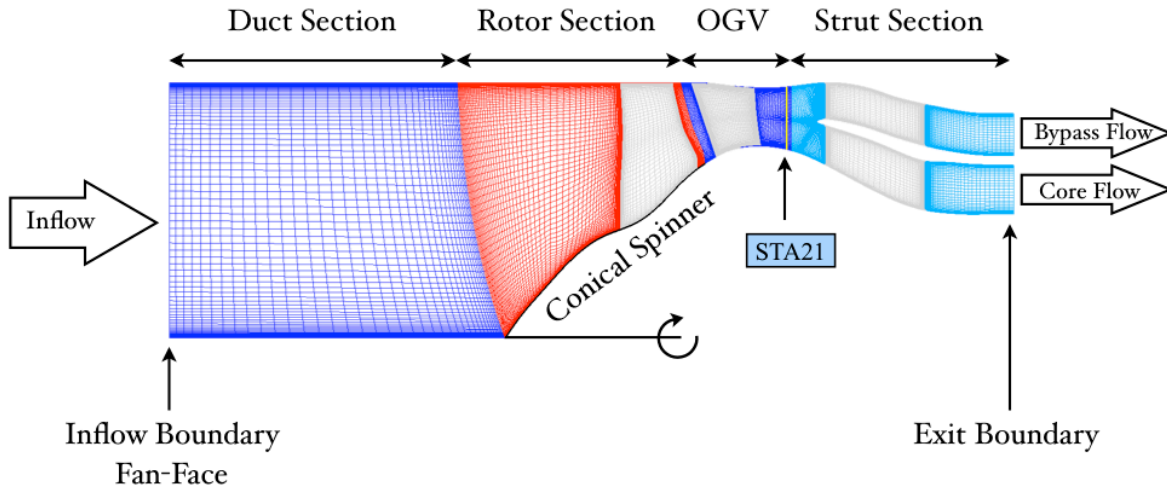
Figure 1. Computational Geometry of the RTA Fan Rig.
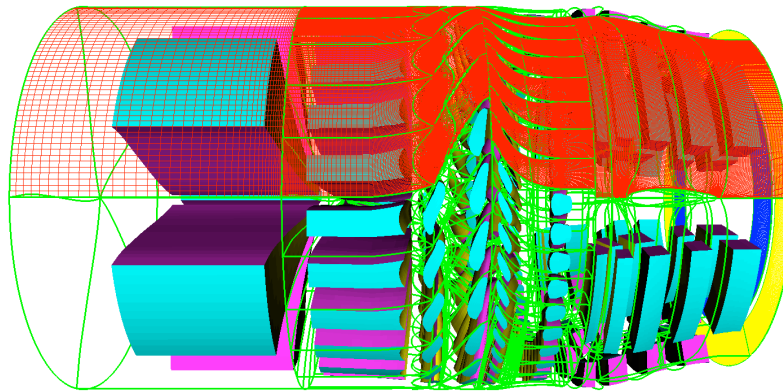
Figure 2. Block Topology for the 230-Block Full Wheel Simulation.

(a)
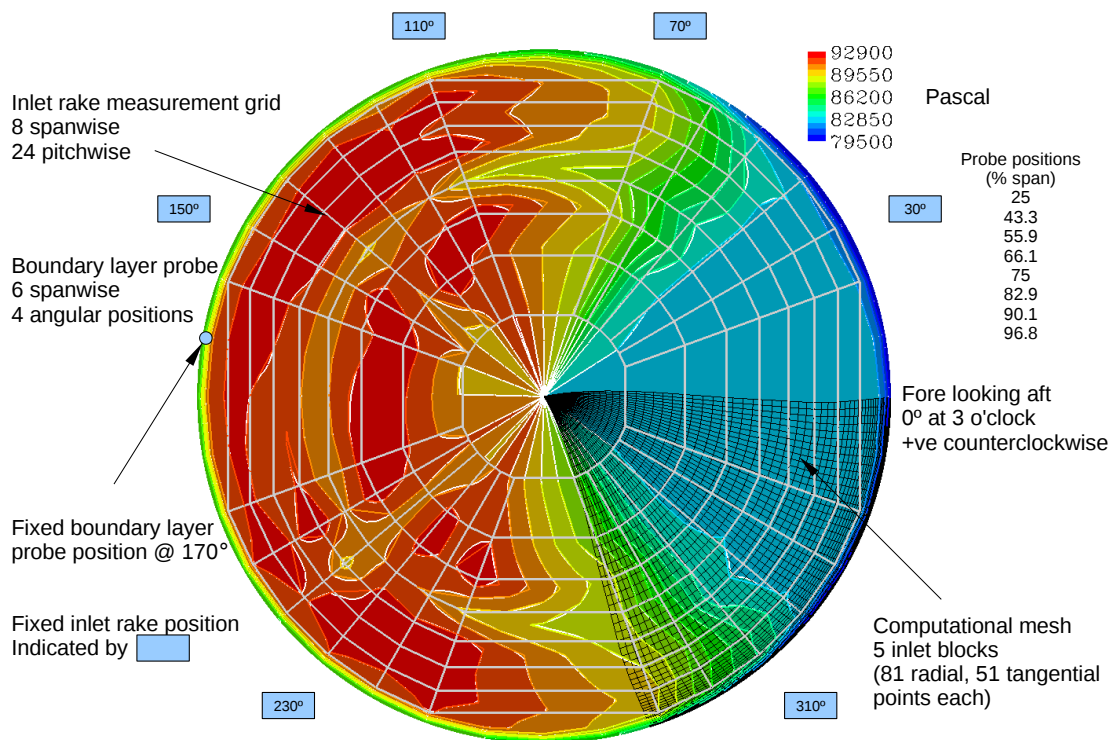
(b)

Figure 3. "Sinusoidal" Screen Generated Total Pressure Field at the Fan-Face.
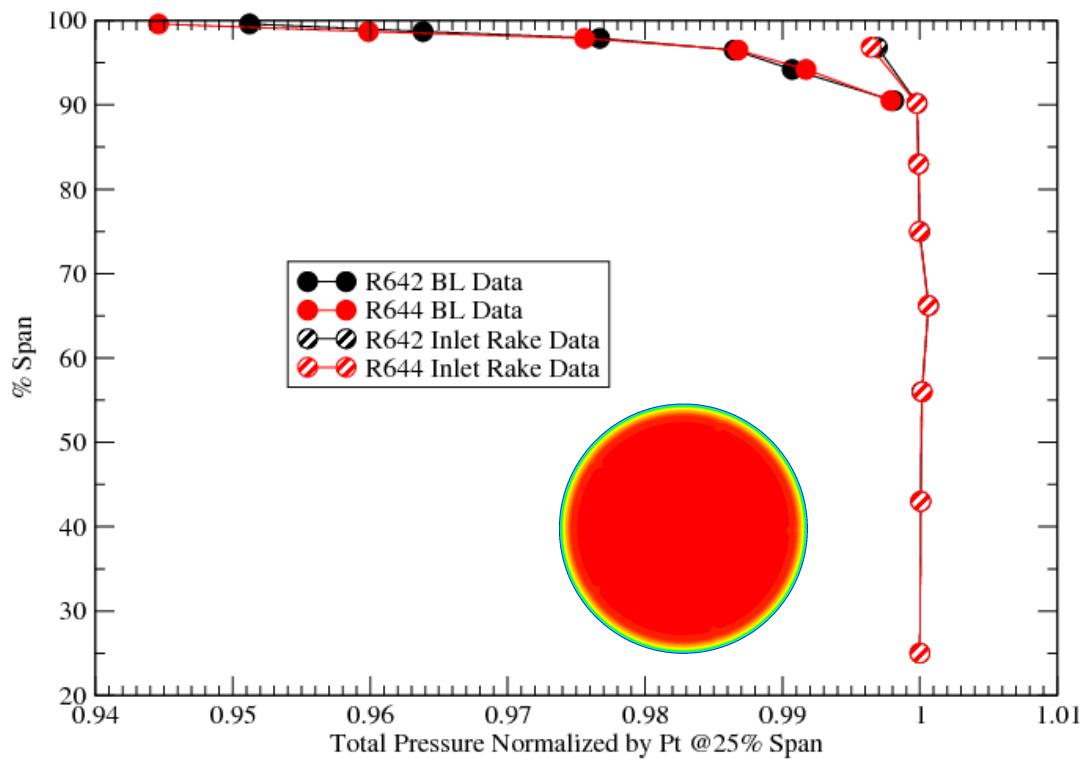
Figure 4. Radial Profile of Total Pressure at the Fan-Face for Uniform Inflow.
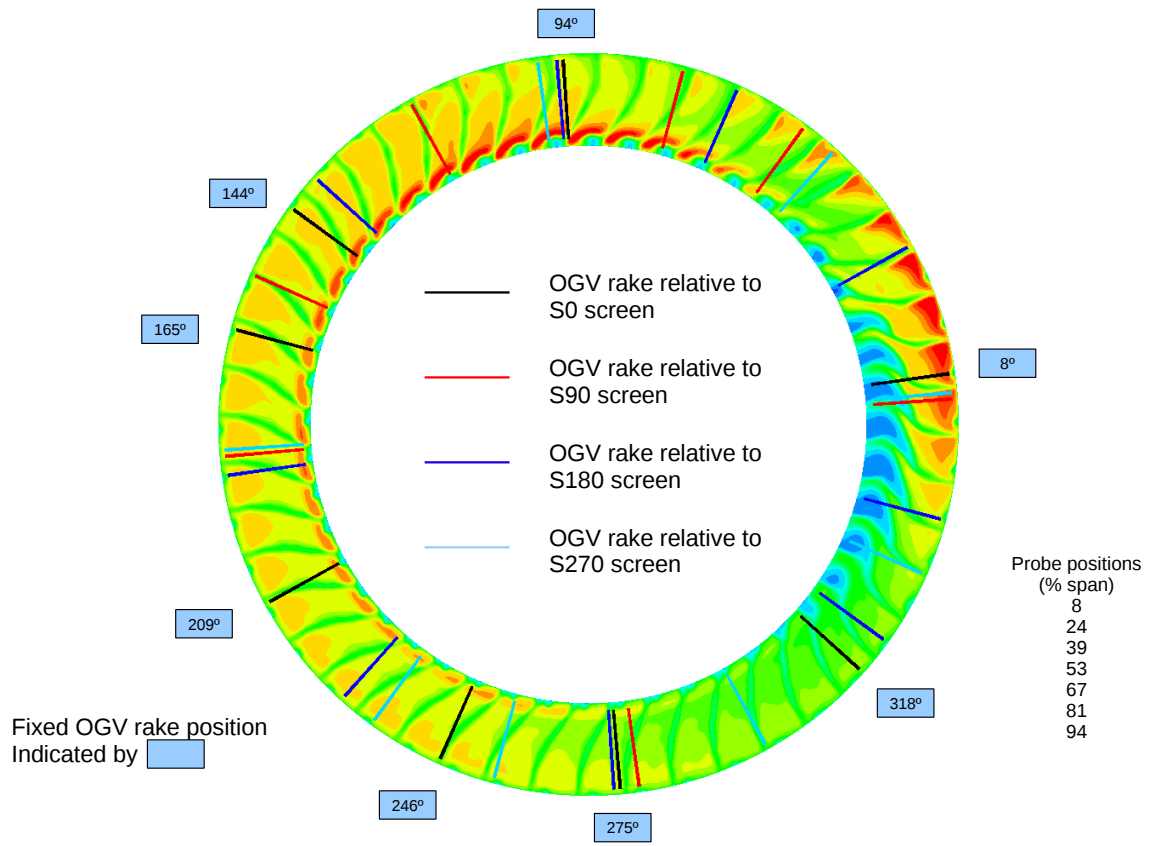
Figure 5. OGV Rake Position.
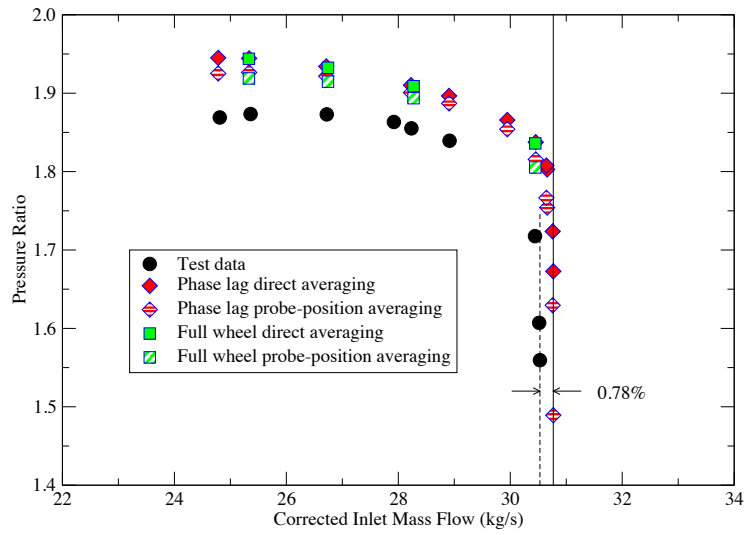
(a) Total Pressure Ratio.
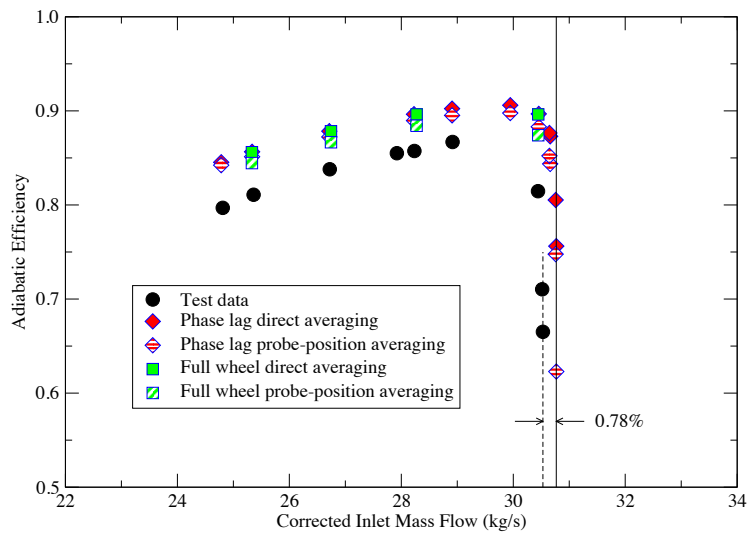
(b) Adiabatic Efficiency.

Figure 6. Comparison of Total Pressure Ratio and Adiabatic Efficiency for Uniform Inflow.
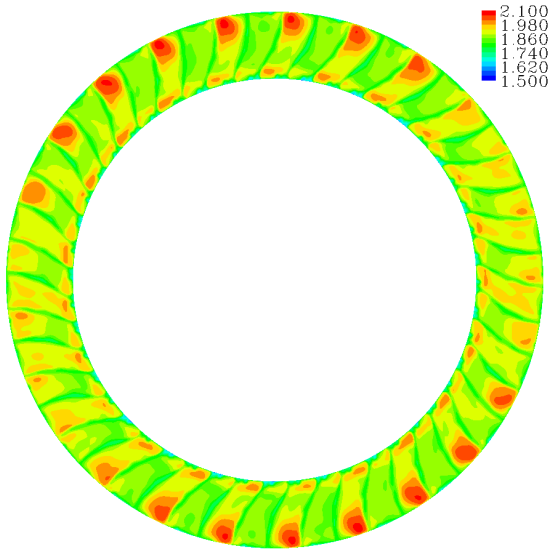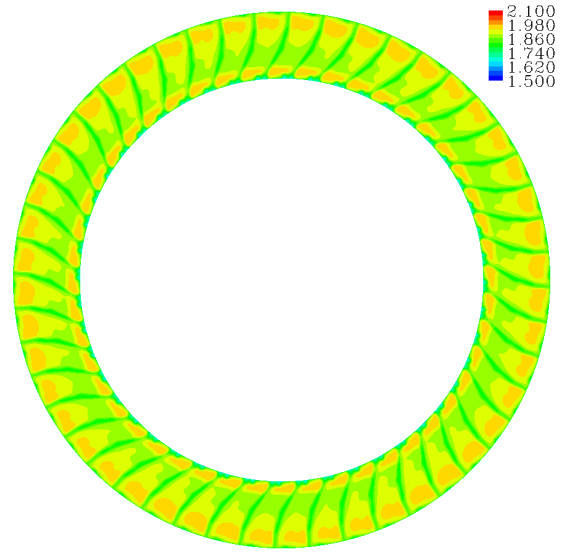
(a) A Snapshot in Time   (b) Time Averaged

Figure 7. Uniform Inflow — Comparison of an Instantaneous and the Time Averaged Total Pressure at STA21 for the Near Design Case (R642).
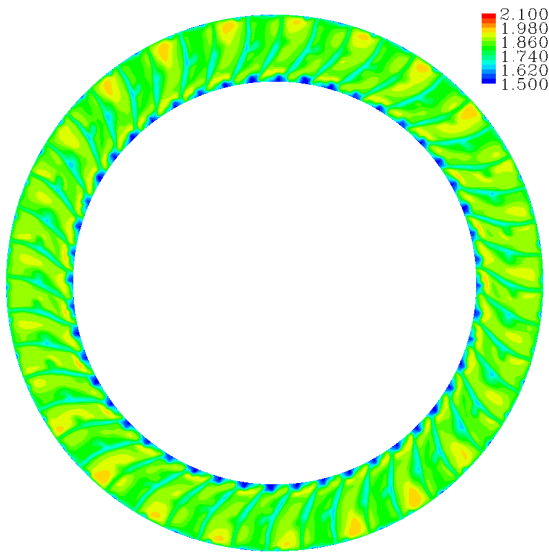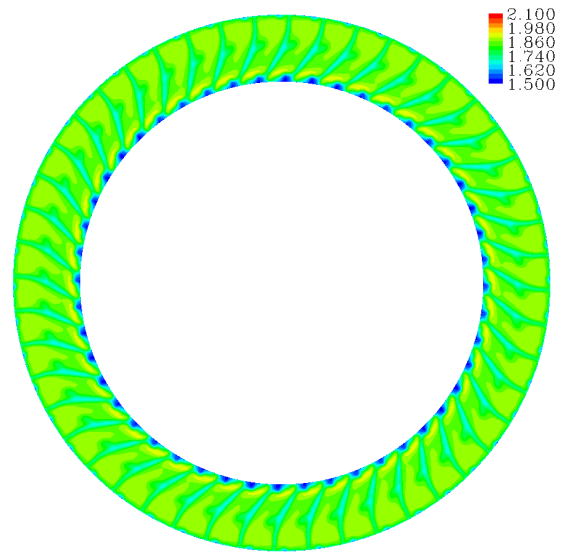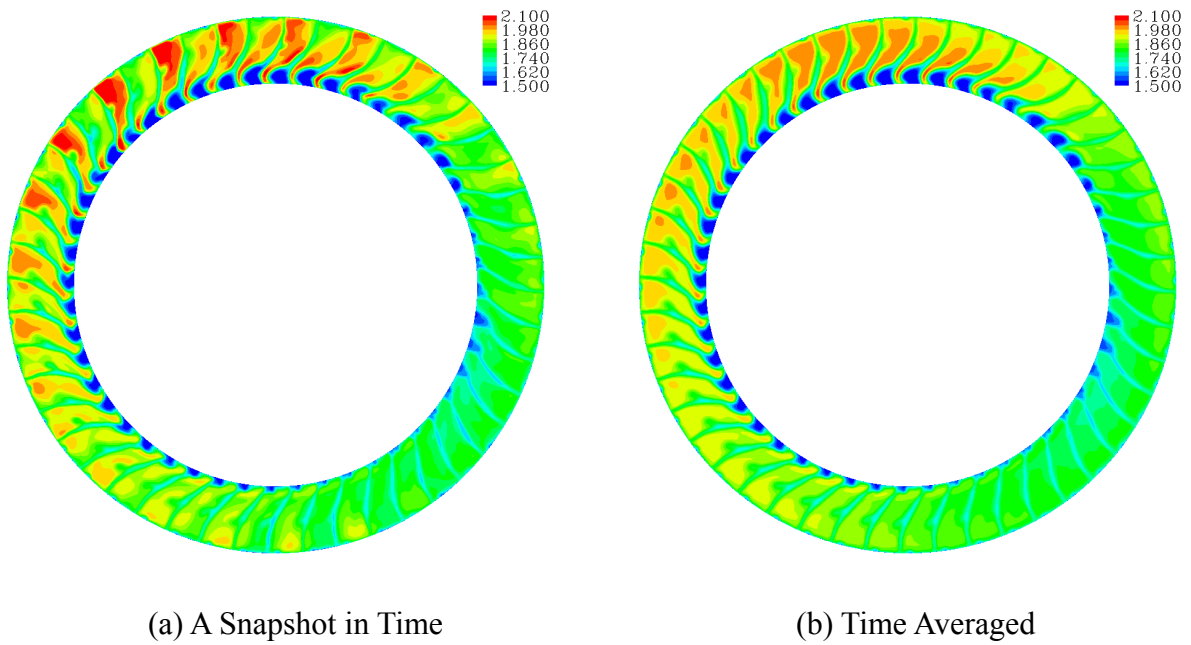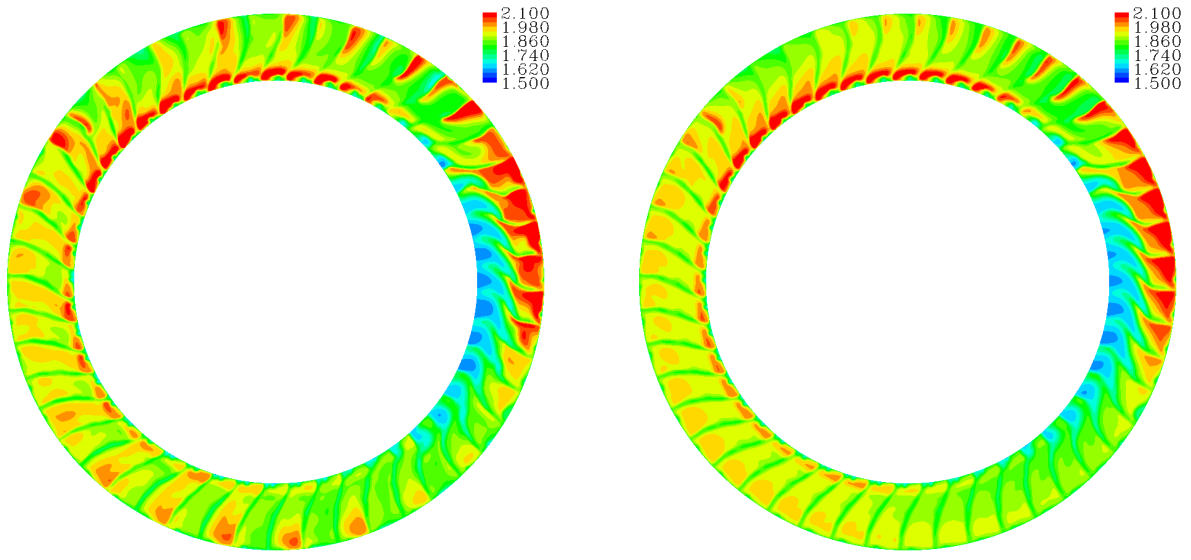

(a) A Snapshot in Time   (b) Time Averaged

Figure 8. Uniform Inflow — Comparison of an Instantaneous and the Time Averaged Total Pressure at STA21 for the Near Choke Case (R645).
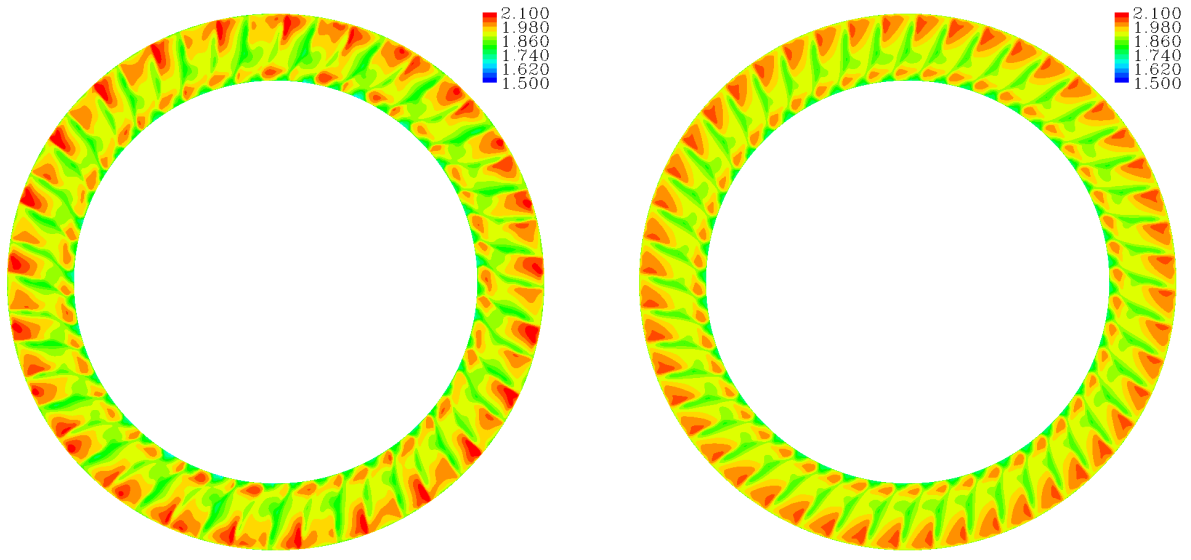
(a) A Snapshot in Time   (b) Time Averaged

Figure 9. Uniform Inflow — Comparison of an Instantaneous and the Time Averaged Total Pressure at STA21 for the Near Stall Case (R649).
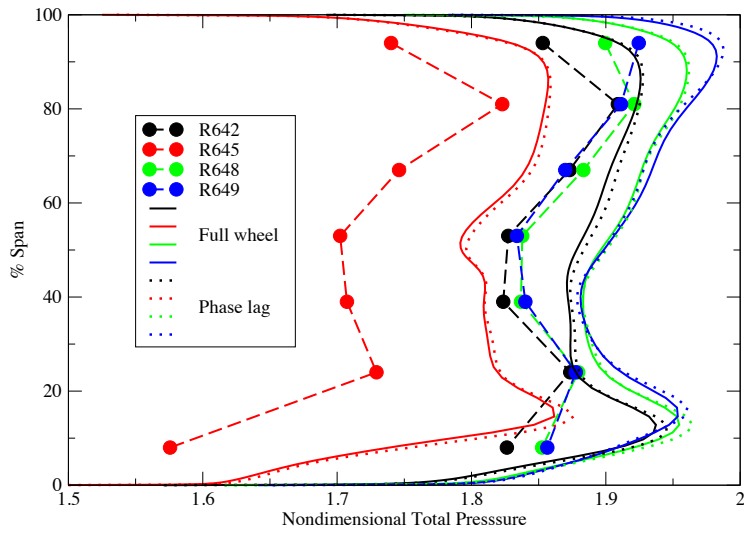
(a) Total Pressure.
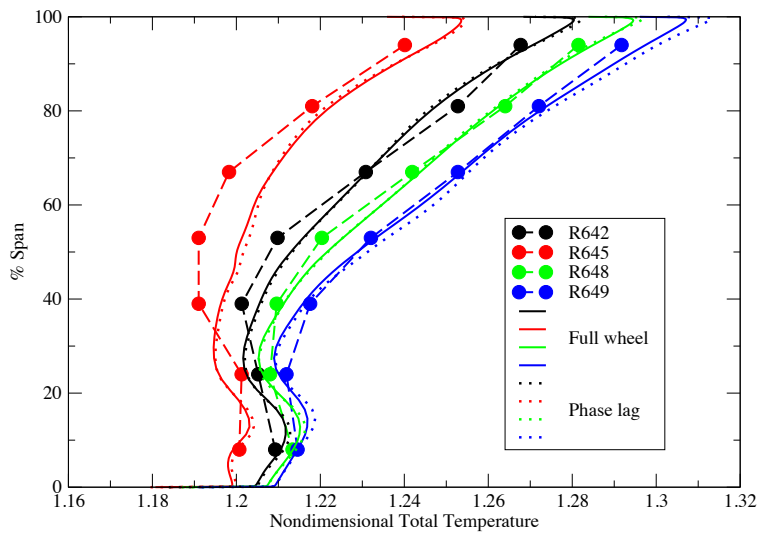
(b) Total Temperature.

Figure 10. Comparison of Radial Profiles of Total Pressure and Total Temperature at STA 21 for Full Wheel and Phase Lag Simulations.
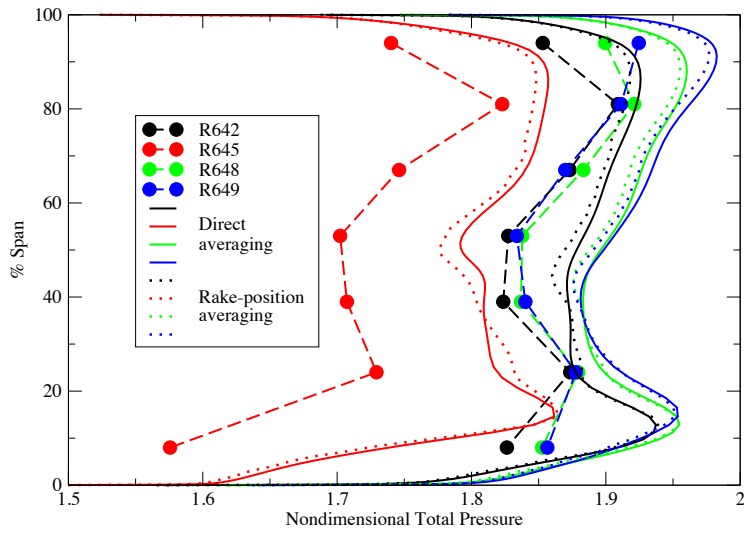
(a) Total Pressure.
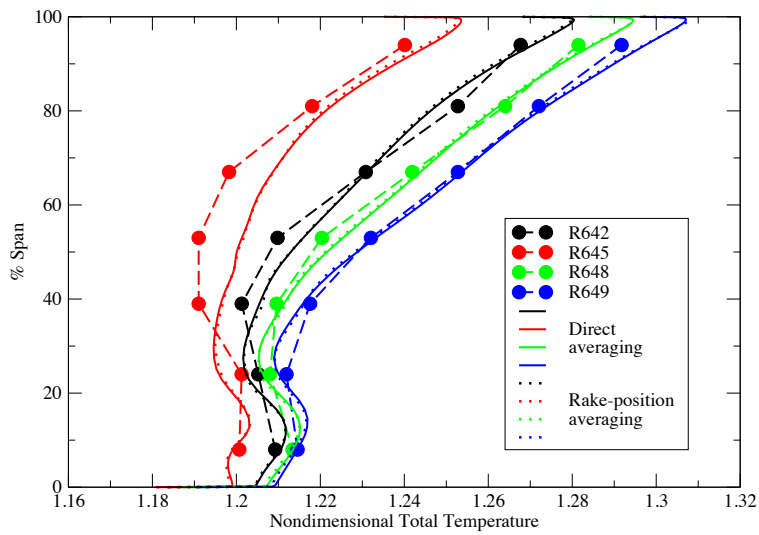
(b) Total Temperature.

Figure 11. Comparison of Radial Profiles of Total Pressure and Total Temperature at STA 21 Computed by the 2 Averaging Methods for the Full Wheel Simulations.
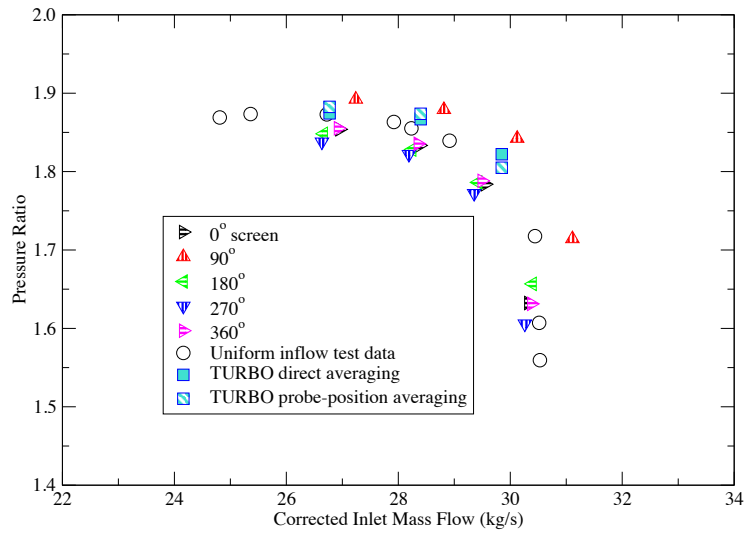
(a) Total Pressure Ratio.
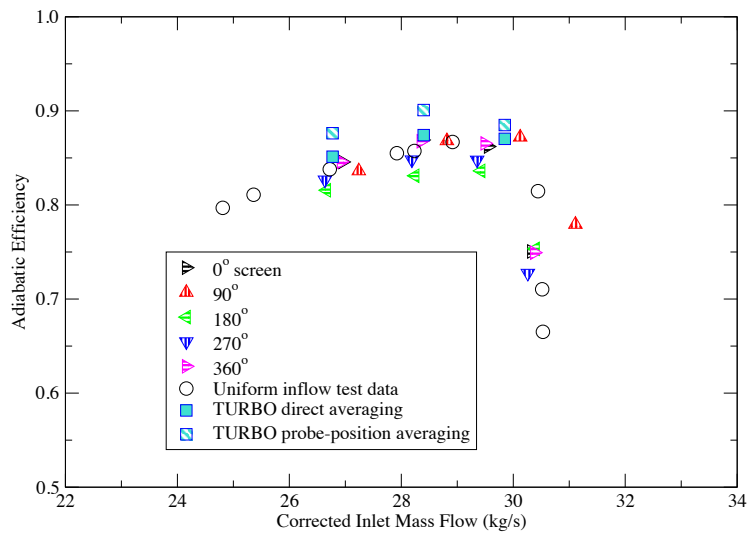
(b) Adiabatic Efficiency.

Figure 12. Comparison of Total Pressure Ratio and Adiabatic Efficiency for Distortion Inflow.

(a) A Snapshot in Time   (b) Time Averaged
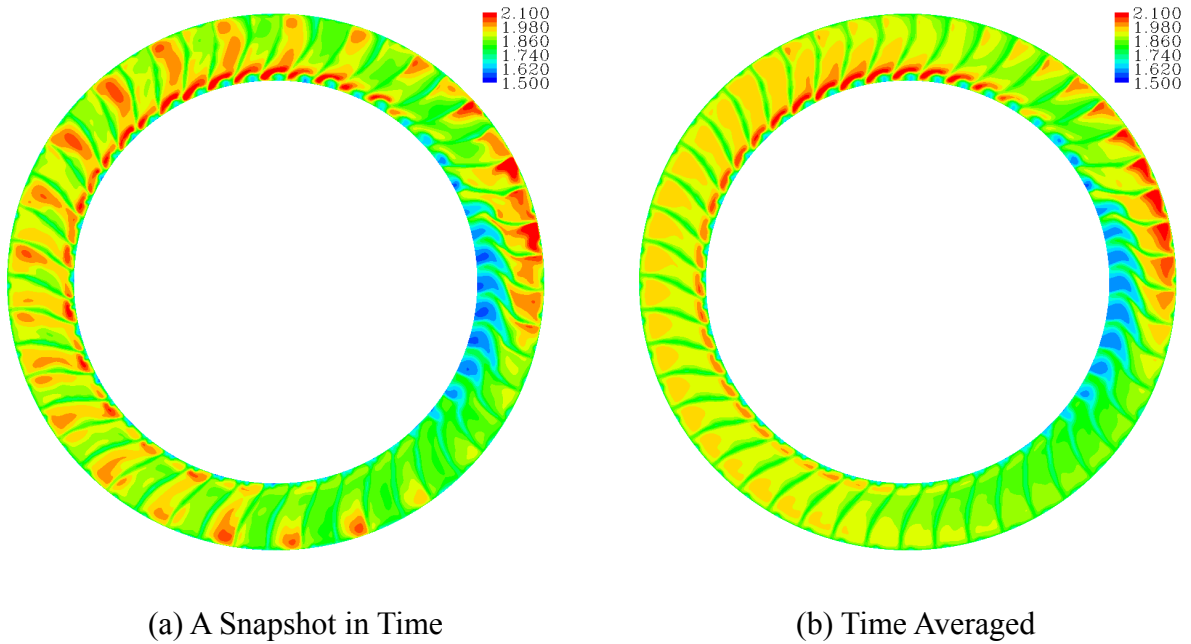
Figure 13. Distortion Inflow ― Comparison of an Instantaneous and the Time Averaged Total Pressure at STA21 for the Near Design Case (R1947-R1951).

(a) A Snapshot in Time   (b) Time Averaged

Figure 14. Distortion Inflow ― Comparison of an Instantaneous and the Time Averaged Total Pressure at STA21 for the Near Choke Case (R1957-R1961).

(a) A Snapshot in Time   (b) Time Averaged

Figure 15. Distortion Inflow ─ Comparison of an Instantaneous and the Time Averaged Total Pressure at STA21 for the Near Stall Case (R1962-R1966).
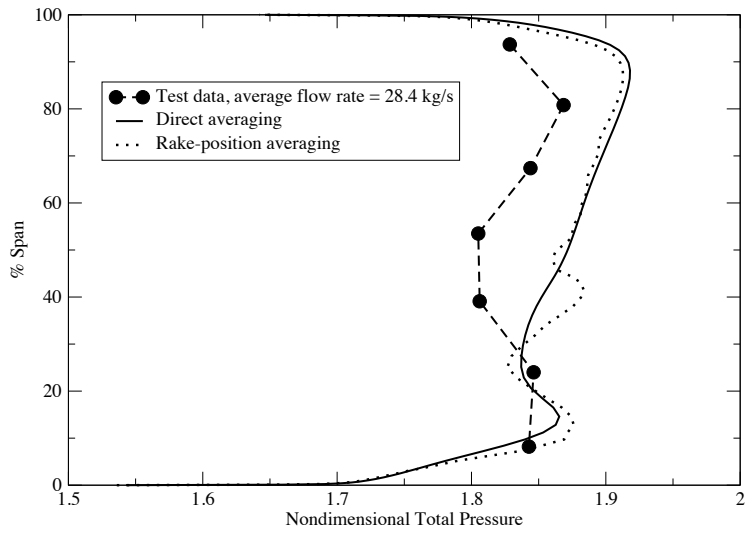
(a) Near Design Case.
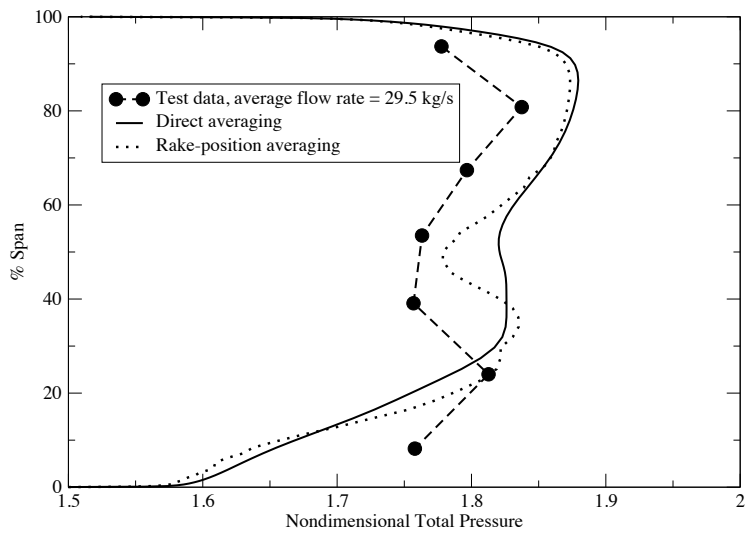
(b) Near Choke Case.
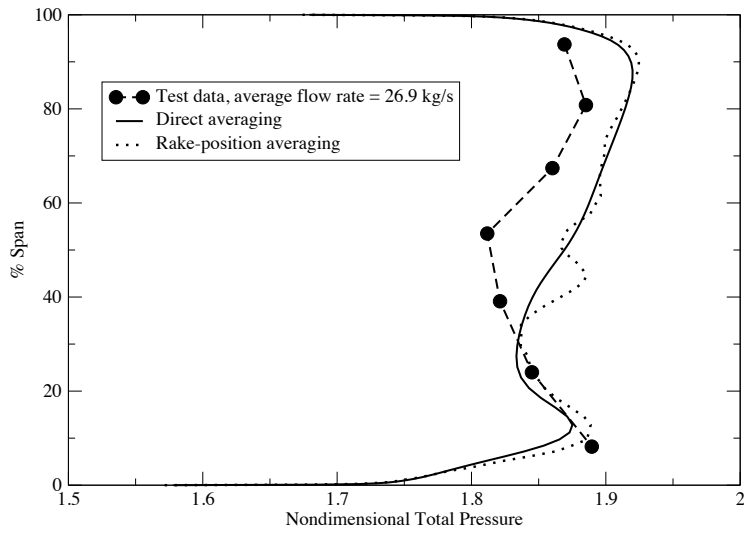
(c) Near Stall Case.

Figure 16. Comparison of Radial Profiles of Total Pressure at STA 21 Computed by the 2 Averaging Methods for the 3 Distortion Inflow Simulations.
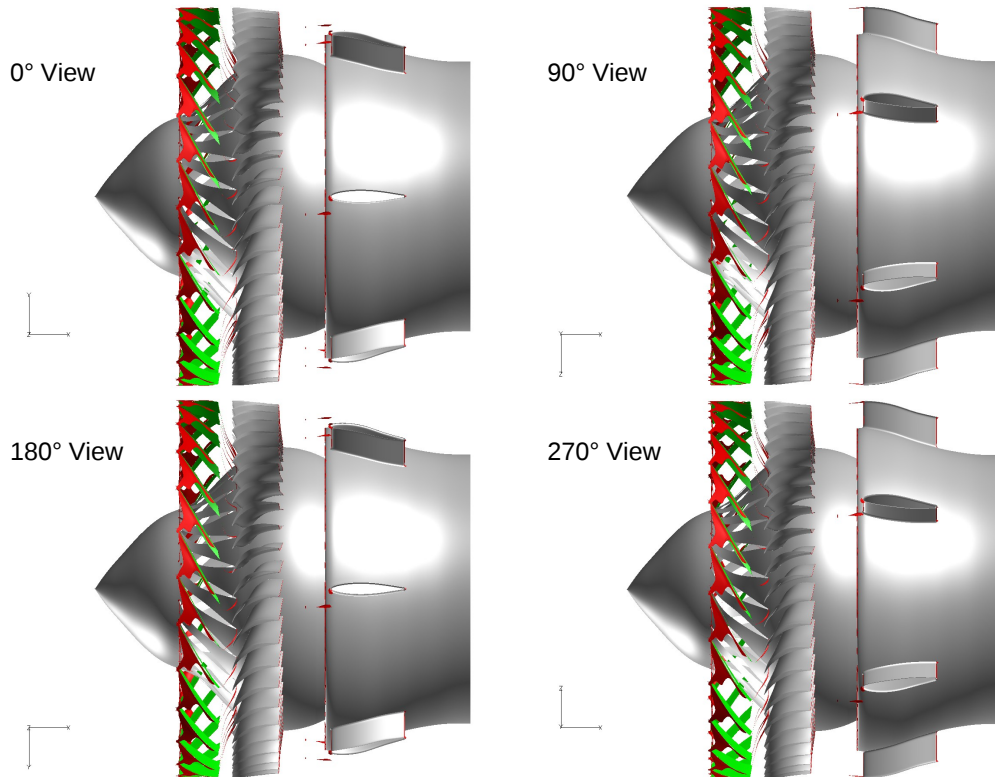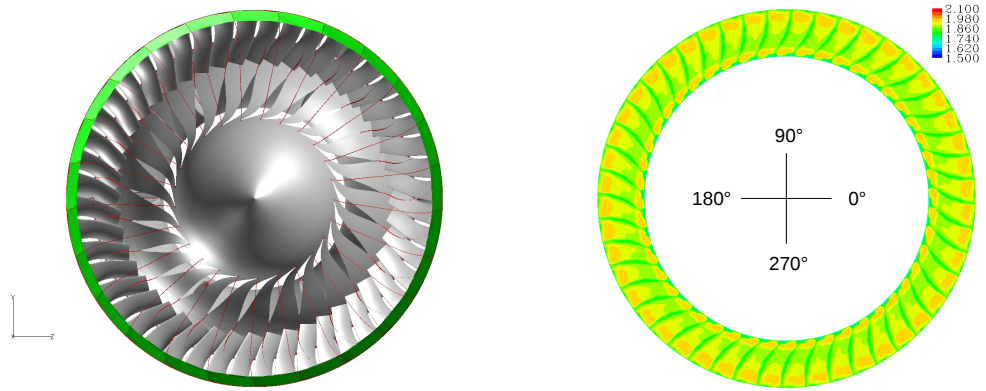
Figure 17. Supersonic (Green) and Separated (Red) Region — Near Design Uniform Inflow.
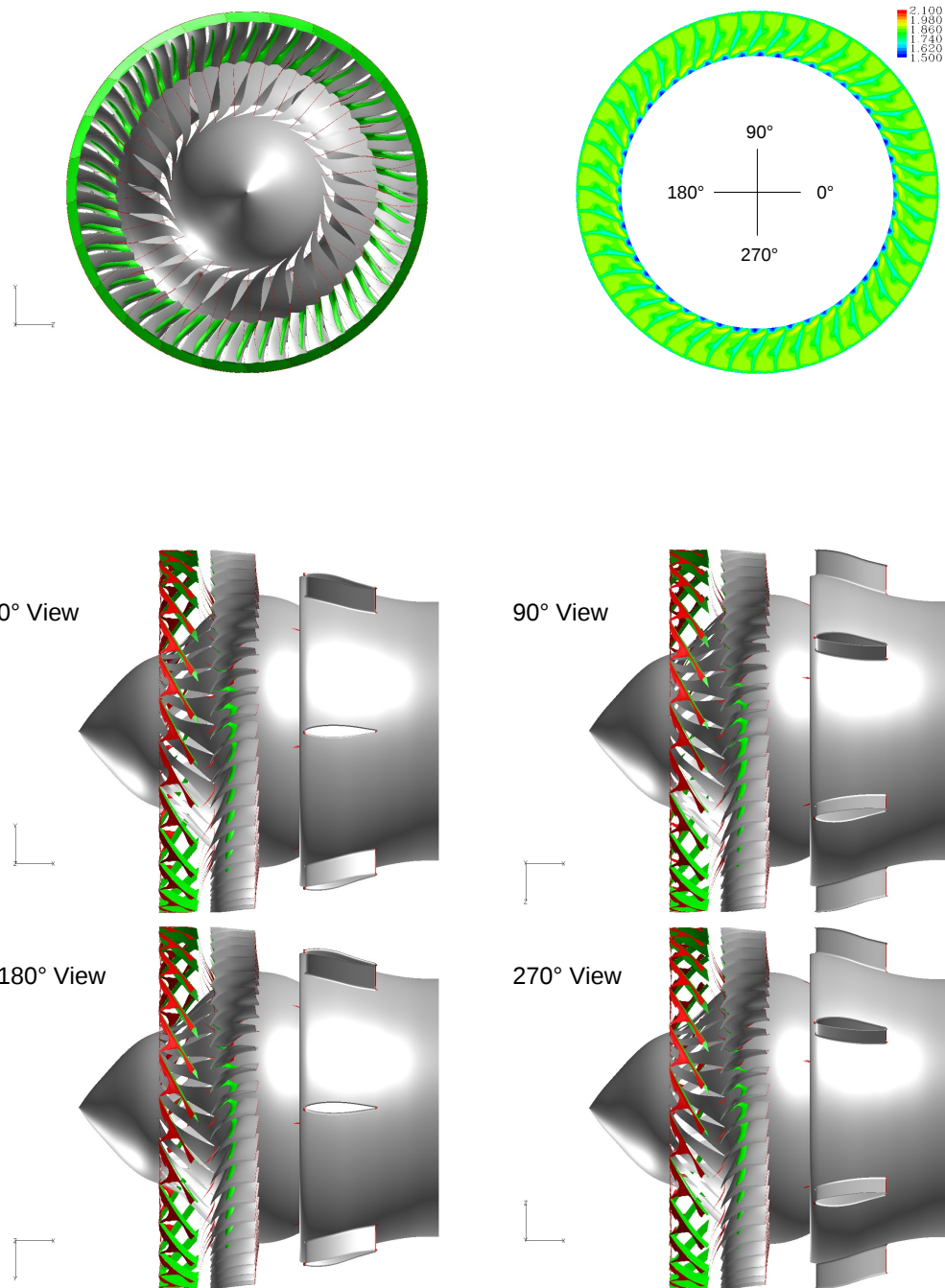
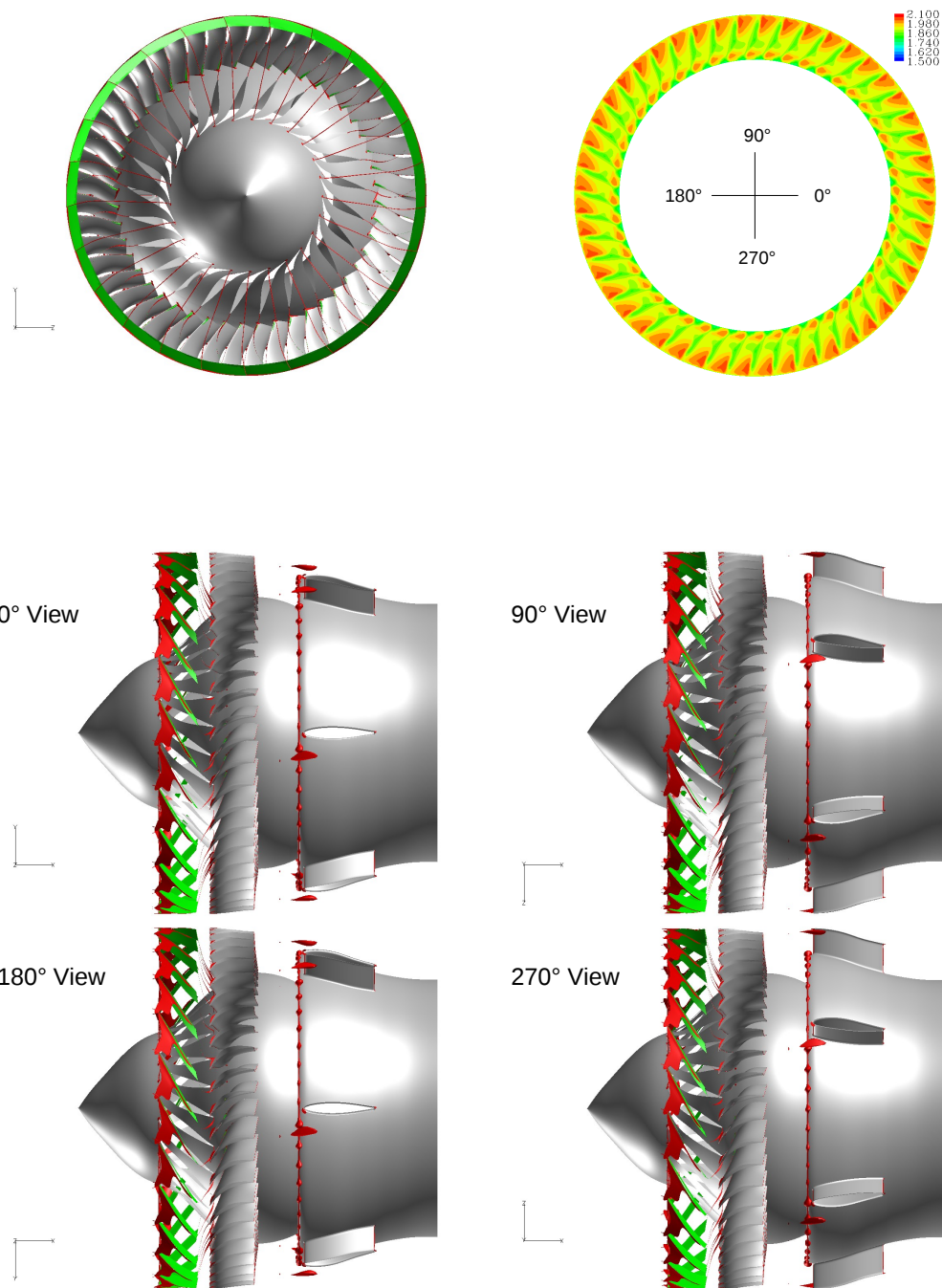Figure 18. Supersonic (Green) and Separated (Red) Region — Near Choke Uniform Inflow.

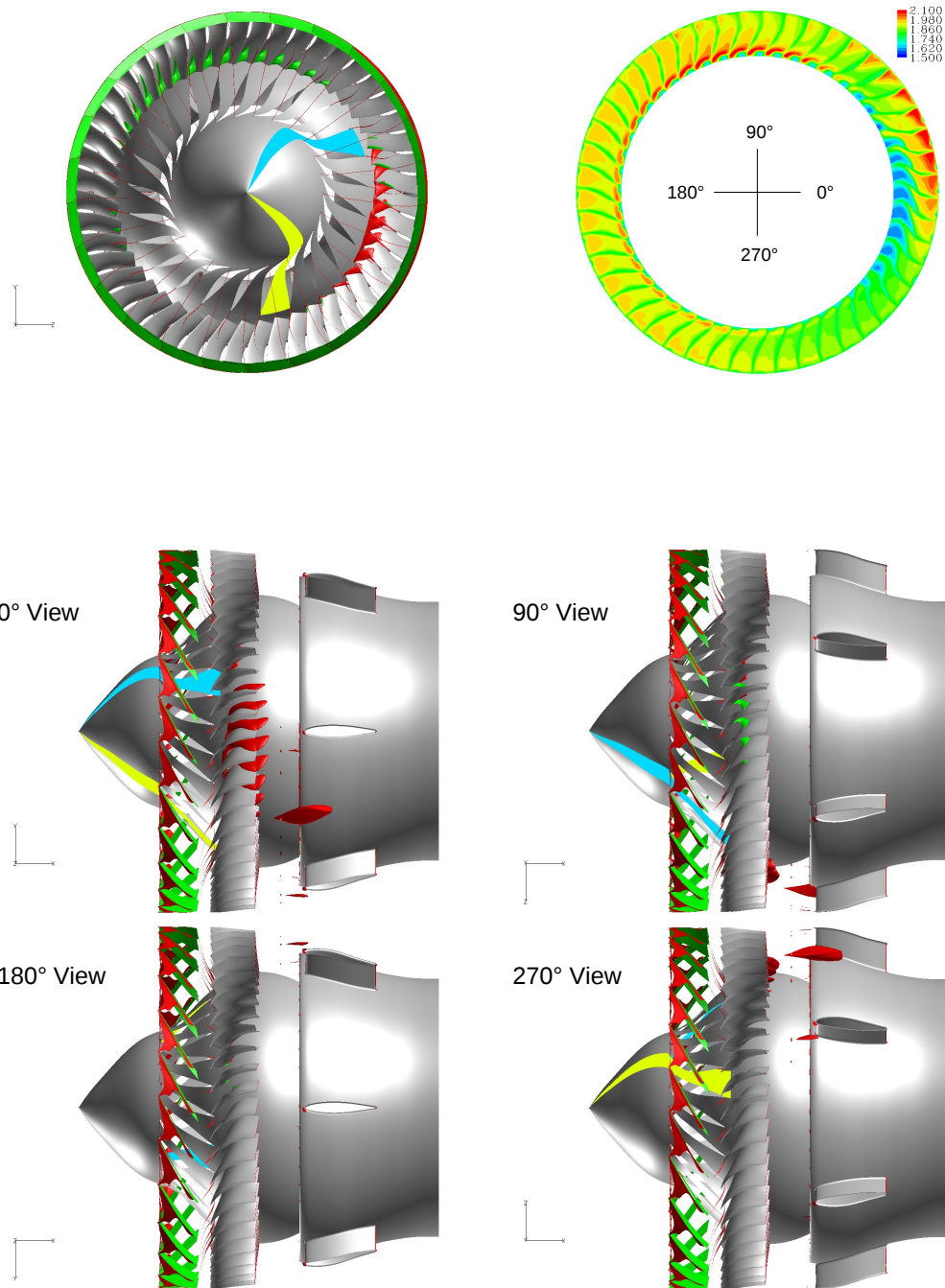Figure 19. Supersonic (Green) and Separated (Red) Region — Near Stall Uniform Inflow.

Figure 20. Supersonic (Green) and Separated (Red) Region — Near Design Distortion Inflow.
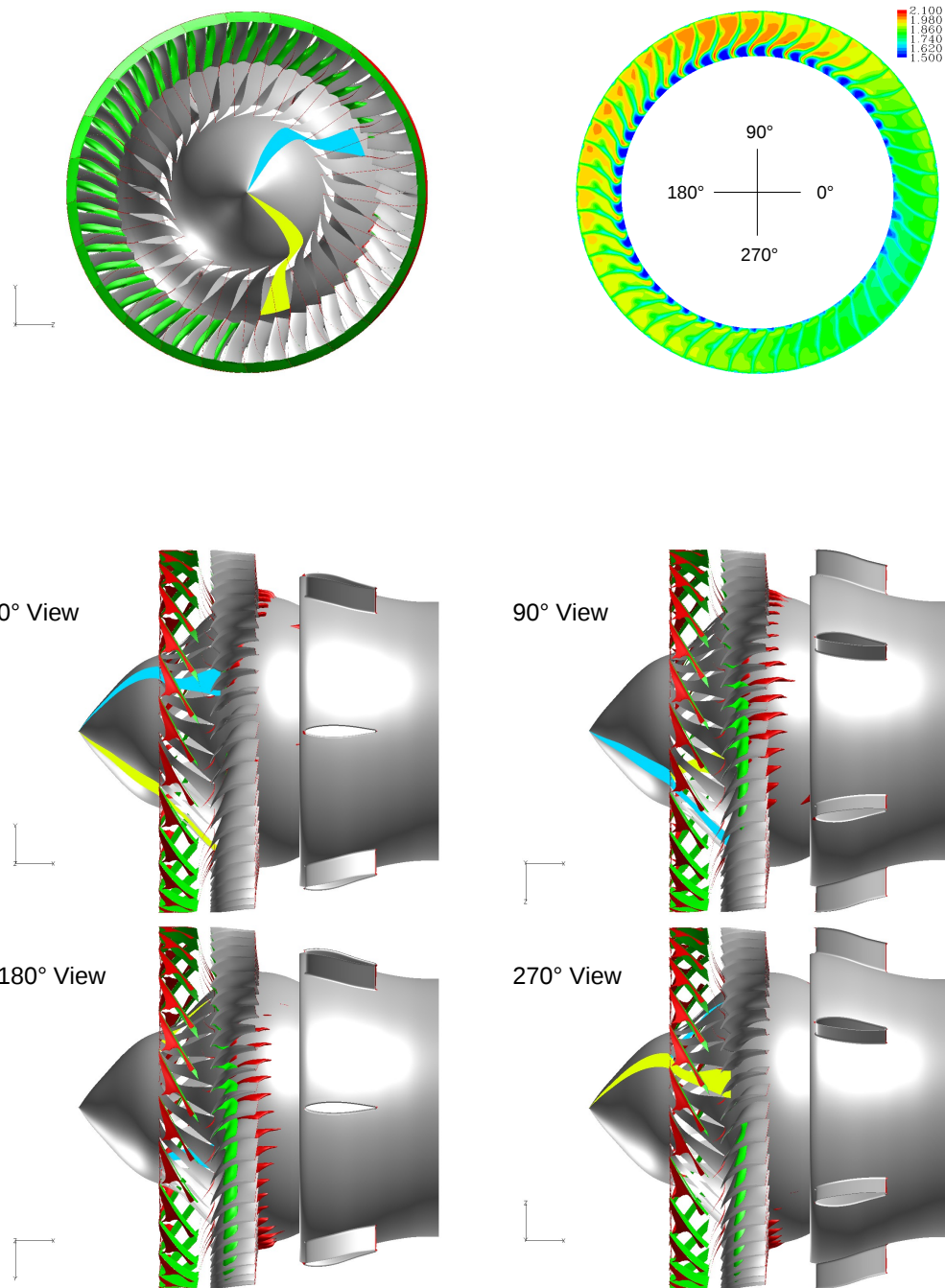
Figure 21. Supersonic (Green) and Separated (Red) Region — Near Choke Distortion Inflow.
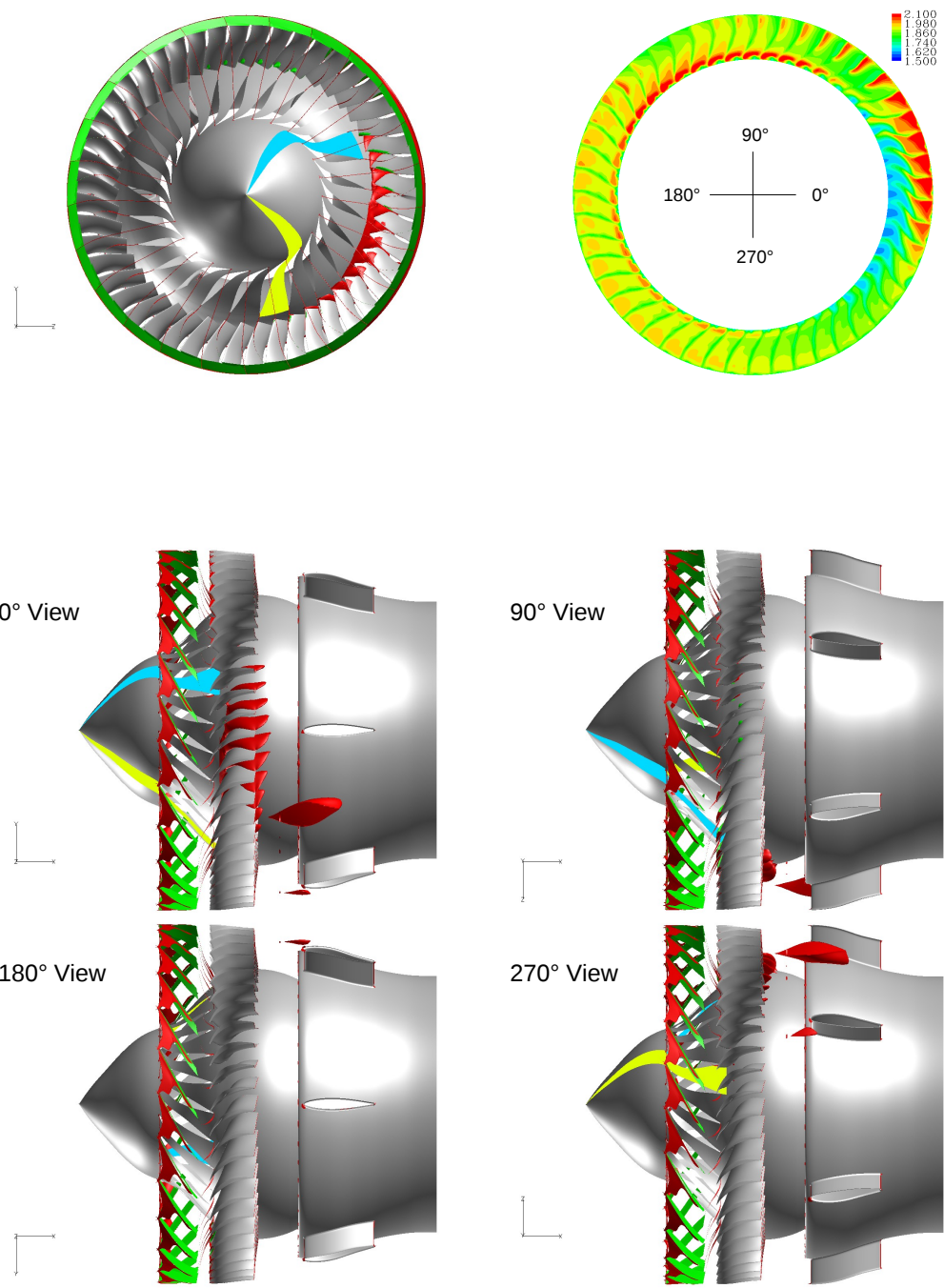
Figure 22. Supersonic (Green) and Separated (Red) Region — Near Stall Distortion Inflow.